Nano Research

ISSN 1998-0124 CN 11-5974/O4
https://doi.org/10.1007/s12274-021-3507-8

Research Article

Vascular-confined multi-passage discoidal nanoconstructs for the low-dose docetaxel inhibition of triple-negative breast cancer growth

Alessia Felici[1,2], Daniele Di Mascolo[1], Miguel Ferreira[1], Simone Lauciello[3], Luca Bono[4], Andrea Armirotti[4], Arunkumar Pitchaimani[1], Anna Lisa Palange[1,§], and Paolo Decuzzi[1,§] (✉)

[1] *Laboratory of Nanotechnology for Precision Medicine, Fondazione Istituto Italiano di Tecnologia, Genoa 16163, Italy*
[2] *Department of Informatics, Bioengineering, Robotics and System Engineering, University of Genoa, Genoa 16126, Italy*
[3] *Nanochemistry Laboratory, Fondazione Istituto Italiano di Tecnologia, Genoa 16163, Italy*
[4] *Analytical Chemistry Laboratory, Fondazione Istituto Italiano di Tecnologia, Genoa 16163, Italy*
[§] *Anna Lisa Palange and Paolo Decuzzi contributed equally to this work.*

Received: 25 September 2020 / **Revised:** 1 April 2021 / **Accepted:** 9 April 2021

ABSTRACT

Taxane efficacy in triple negative breast cancer (TNBC) is limited by insufficient tumor accumulation and severe off-target effects. Nanomedicines offer a unique opportunity to enhance the anti-cancer potency of this drug. Here, 1,000 nm × 400 nm discoidal polymeric nanoconstructs (DPN) encapsulating docetaxel (DTXL) and the near infrared compound lipid-Cy5 were engineered. DPN were obtained by filling multiple times cylindrical wells in a poly(vinyl alcohol) template with a polymer mixture comprising poly(lactic-co-glycolic acid) (PLGA) and poly(ethylene glycol) diacrylate (PEG-DA) chains together with therapeutic and imaging agents. The resulting "multi-passage" DPN exhibited higher DTXL loading, lipid-Cy5 stability, and stiffness as compared to the conventional "single-passage" approach. Confocal microscopy confirmed that DTXL-DPN were not taken up by MDA-MB-231 cells but would rather sit next to the cell membrane and slowly release DTXL thereof. Empty DPN had no toxicity on TNBC cells, whereas DTXL-DPN presented a cytotoxic potential comparable to free DTXL (IC_{50} = 2.6 nM ± 1.0 nM vs. 7.0 nM ± 1.09 nM at 72 h). In orthotopic murine models, DPN accumulated in TNBC more efficiently than free-DTXL. With only 2 mg/kg DTXL, intravenously administered every 2 days for a total of 13 treatments, DTXL-DPN induced tumor regression and were associated to an overall 80% survival rate as opposed to a 30% survival rate for free-DTXL, at 120 days. All untreated mice succumbed before 90 days. Collectively, this data demonstrates that vascular confined multi-passage DPN, biomimicking the behavior of circulating platelets, can efficiently deliver chemotherapeutic molecules to malignant tissues and effectively treat orthotopic TNBC at minimal taxane doses.

KEYWORDS

hydrogel particles, template strategy, vascular targeting, biomimicry, cancer therapy

1 Introduction

Breast cancer is the most common malignancy in females and the second leading cause of cancer-related deaths [1]. About 20% of breast cancers are negative for both hormones–estrogen and progesterone, and HER2 receptors. This phenotype characterizes the breast malignancy with the most dismal prognosis, known as the triple negative breast cancer (TNBC) [2], showing a faster growth rate and higher likelihood of relapse at secondary sites as compared to hormone positive breast cancers [3]. As hormones and HER2 are not fueling cancer growth, TNBC are unresponsive to typical endocrine therapies. Consequently, the poor outcome of TNBC patients is also attributed to the limited availability of effective therapeutic strategies [4, 5]. In addition, the significant tumor heterogeneity in TNBCs has hindered the success of targeted medicines, such as tamoxifen and Herceptin [6]. Therefore, TNBC treatment still remains a challenge and, to date, the combination of surgery, radiation therapy, and chemotherapy is the sole option for primary mases [7–9], whereas systemic chemotherapy is used for attacking metastatic niches [10]. Among the plethora of clinically approved chemotherapeutic molecules, docetaxel (DTXL) is one of the most potent but is also responsible for severe adverse reactions due to its non-specific accumulation in healthy tissues [11] and the need of toxic solubilizing agents [12, 13]. For this, the administered doses are often limited, thus significantly impairing the DTXL cytotoxic activity within the tumor tissue [14, 15].

In this scenario, nanomedicine could play a fundamental role to enhance the therapeutic efficacy of small anti-cancer molecules optimizing their bioavailability, tissue deposition, and cellular uptake while limiting off-site targeting [16–19]. Traditionally, spherical nanoparticles with a sufficiently small size (<200 nm) have been designed to cross the hyperpermeable tumor vasculature, thus relying on the well-known enhanced permeability and retention (EPR) effect [20, 21]. By passing through the "fenestrated" endothelium, spherical nanoparticles can reach the tumor parenchyma and progressively accumulate

Address correspondence to paolo.decuzzi@iit.it

therein, given the lack of a functional lymphatic drainage. A variety of EPR-dependent delivery systems for taxanes have been designed in the context of TNBC therapy, including macromolecular conjugations [22], liposomes [23], polymeric nanoparticles [24–26], micelles [27], and prodrugs [28]. Some of these platforms are already approved for clinical use or under clinical investigation [19, 29]. For instance, the albumin-bound (nab)-paclitaxel (Abraxane) was approved by Food and Drug Administration (FDA) in 2005 as a second-line treatment of metastatic breast cancer [18]. Interestingly, the clinical use of Abraxane is associated with lower systemic toxicity and only a modest improvement in the therapeutic index [18, 30]. Other taxane-loaded polymeric micelles and nanoparticles, at different stages of clinical development, presented similar outcomes for both primary and metastatic TNBC [27, 31–33]. Recently, Contreras-Cáceres et al. developed a pH-sensitive nano-carrier encapsulating paclitaxel within the hollow structure of oxidized poly(4-vinyl pyridine) and demonstrated an improved antitumor activity on A-549 and MCF-7 multicellular tumor spheroids (MTS) [34], as compared to the free drug. In other nanoparticle formulations, a targeting moiety was included on the nanoparticles' surface to enhance tumor accumulation and deep penetration into the malignant mass [17, 35–37]. The cell receptor CD44 has been extensively investigated as a targeting molecule in TNBC. For instance, Huang et al. demonstrated that CD44-targeted DTXL-loaded nanoparticles have enhanced antitumor activity over the untargeted nanoparticles [35]. De-Sheng Liang and colleagues implemented a dual targeting approach including on the same nanoparticle moieties to recognize CD44 molecules, expressed on the cancer cells, and neuropilin receptors, exposed on the tumor neovasculature. This approach succeeded in suppressing tumor cell invasiveness and metastatic potential [36]. Also, epidermal growth factor receptor (EGFR)-targeted immunoliposomes labeled with Technetium-99m were shown to highly accumulate in MDA-MB-231 xenografts and in the metastatic lymph nodes of nude rats by single photon emission computed tomography (SPECT/CT) imaging [37].

For all the above listed nanoparticles, and the many more proposed in the open literature, tumor accumulation via the EPR effect has been always sufficient to modulate disease progression or even induce regression. However, these encouraging preclinical results often have not been recapitulated in clinical settings for a number of reasons. First, the permeability of the tumor neovasculature to nanoparticles is highly heterogeneous, both at the intra- and inter-patient levels [21, 38–40]. Second, targeting may improve nanoparticle retention in tumors, but could also favor sequestration by cells of the immune system [41]. Furthermore, bio-conjugation may not be that intrinsically specific because targeting receptors could also be expressed on healthy cells or the moieties' orientation over the particle surface could be sub-optimal thus impairing the proper biological recognition. Along this line, a recent meta-analysis revealed that active targeting agents yield only modest improvements in intratumor nanoparticle accumulation [38]. In this scenario, designing particles to target and accumulate within the tumor vasculature without relying on the EPR effect could be a valuable, complementary strategy [42–45]. The tumor vasculature is tortuous and characterized by lower flow rates as compared to healthy vascular beds. This specific hemodynamic conditions and vascular architecture would favor the deposition of non-spherical micrometric particles over more conventional spherical nanoparticles [45–48]. These micrometric particles would mimic the behavior of circulating platelets, thus confirming the importance of bioinspiration and biomimicry in the development of novel drug delivery systems [49]. Indeed, the authors have previously demonstrated that discoidal particles can lodge within the tortuous and low perfused tumor microvasculature, up to 20% of the injected dose [45].

Here, the authors developed a novel class of discoidal polymeric nanoconstructs (DPN) to boost drug loading and release at the targeted site without relying on the EPR effect. Specifically, 1,000 nm × 400 nm DPN were directly loaded with the potent anti-cancer drug DTXL and realized using a "multi-passage" loading strategy. A comparison between the "multi-passage" and "single-passage" DPN is first presented in terms of morphological, physico-chemical, and *in vitro* pharmacological characterizations. Then, the therapeutic efficacy and imaging efficiency of DTXL and Cy5-loaded DPN is tested preclinically in mice bearing an orthotopic model of triple negative breast cancer.

2 Experimental methods

2.1 Chemicals

Polydimethylsiloxane (PDMS) (Sylgard 184) was purchased from Dow Coming Corp (Midland, USA). Poly(vinylalcohol) (PVA, M_W 31,000–50,000), poly(DL-lactide-coglycolide) acid (PLGA, lactide:glycolide = 50:50, M_W 38,000–54,000), poly(ethylene glycol) diacrylate (Mn 750) (PEG-DA), and 2-hydroxy-40-(2-hydroxyethoxy)-2-methylpropiophenone (photo-initiator) were purchased from Sigma-Aldrich (Missouri, USA). 1,2-Dipalmitoyl-sn-glycero-3-phosphoethanolamine-N-(lissamine rhodamine B sulfonyl) (ammonium salt) (RhB-DSPE) was purchased from Avanti Polar Lipids (Alabama, USA). DTXL and paclitaxel (PTXL) were purchased from Alfa Easer (Massachusetts, USA).

2.2 Methods

Fabrication of DPN. DPN were synthetized using a top-down fabrication strategy described in details in previous works by the authors [50, 51]. Briefly, the process started with the fabrication of the silicon master template via Laser Writer Lithography. This technique was used to imprint on a silicon wafer a specific pattern of wells with the geometry of the final DPN. Then, a solution composed by polydimethylsiloxane (PDMS) (Sylgard 184, 10-parts base elastomer and 1-part curing agent) was cast over the silicon wafer to reproduce a negative replica of it. Finally, a sacrificial template was realized by pouring a 5% w/v poly(vinyl alcohol) (PVA) solution on the PDMS template and letting the solution drying at 60 °C for about 3 h. Once polymerized, the hydrophilic PVA template reproduced the same cylindrical holes of the original silicon master. DPN were synthetized using a mixture of PLGA and PEG-DA polymers. 50 mg of PLGA are dissolved in 1 mL of Acetonitrile and mixed with 6 mg of PEG-DA and 10 mg of DTXL. Then, 0.6 mg of a photo-initiator(2-Hydroxy-4'-(2-hydroxyethoxy)-2-methylpropiophenone) were added into the polymeric solution to allow the crosslinking of PEG-DA chains after exposure to ultraviolet (UV)-light (366 nm). A fixed volume of polymeric mixture, including DTXL (5 μL), was then spread through a blade over the PVA template to accurately fill each well. This step was performed one time for the "single-passage" DPN and about 4–5 times till complete solvent evaporation for the "multi-passage" DPN. Finally, the DPN were released from the hydrophilic PVA templates upon dissolution in deionized water for 3 h under gentle stirring, were collected through centrifugation (3,900 rpm for 20 min) and purified from residual debris and scum layer through 2 μm

filtration (Sterlitech).

Physio-chemical characterization. The DPN geometry and synthesis yielding was assessed through Multisizer 4E Coulter Particle Counter (Beckman Coulter, USA) that calculates particle concentration in a defined volume of 20 mL of isotone solution. The hydrodynamic diameter and surface electrostatic charge (ζ potential) of DPN were measured using a Zetasizer Nano (Malvern, UK). The characteristic discoidal shape of DPN was confirmed using electron microscopy. DPN morphology was observed using a Jem-1011 transmission electron microscopy (TEM) (Jeol, Japan) coated with spattered carbon and scanning electron microscopy (SEM) (Helios Nanolab 650) after 10 nm aureum coating. Fluorescent DPN were synthesized by adding 30 μg of rhodamin-B (DSPE-RhB) to the polymeric mix made of PLGA and PEG-DA and were observed using an A1 confocal fluorescent microscope (Nikon).

Mechanical proprieties. The apparent Young's modulus, of single-passage and multi-passage DPN was assessed using the Chiaro nanoindenter system (Optics11). A spherical tip of 3.5 μm in radius and 0.05 N/m stiffness was used to indent the particles. The stiffness of single-passage and multi-passage DPN was determined in liquid (milliQ water) by performing a surface-normal indentation of the single particle fixed on a poly-lysine glass coated. For every indentation, the Hertzian model was used to fit the force-displacement curve from initial DPN surface contact up to 50-nm indentation, to avoid mechanical interference from the underlying substrate.

Loading and release studies. The "direct loading" method was used to uniformly disperse imaging and therapeutic agents within the DPN matrix [51, 52]. Specifically, a 5 μL of homogenous drug/polymer solution was uniformly spread using a blade over the surface of a 3 cm × 3 cm PVA template, containing about 10^8 wells. This step was performed only once for the "single-passage" DPN and several times till complete solvent evaporation for the "multi-passage" DPN. This loading strategy is different from the "absorbance loading" previously described by the authors [51]. The amount of drug loaded within DPN was calculated using a high performance liquid chromatography (HPLC) and by reading the characteristic DTXL UV absorbance at 230 nm (Agilent 1260 Infinity, Germany). Samples for HPLC analysis were prepared by spinning down DPN at 12,700 rpm for 20 min, drying the pellet overnight and dissolving the particles upon incubation with acetonitrile (ACN). The encapsulation efficiency was calculated considering the percentage weight ratio between the drug amount loaded within the DPN matrix at the end of the synthesis process and the initial drug input. Release studies were performed in a volume of 4 L of buffer at controlled pH 7.4 and 37 °C to reproduce typical physiological conditions. At each time point, 200 μL of DPN solution was poured into Slide-A-Lyzer MINI dialysis cups with a molecular cut off of 10 kDa (Thermo Scientific) and dialyzed. At each time point, DPN were collected and dissolved in ACN to read the amount of DTXL still entrapped in the matrix overtime.

***In vitro* cell viability tests.** For cytotoxicity tests *in vitro*, the human TNBC cell line MDA-MB231 was obtained from the American Type Culture Collection (ATCC). Cells were cultured in Eagle's minimal essential medium (EMEM) (ATCC, USA) completed with 10% fetal bovine serum (FBS) (Gibco, Thermo Fisher Scientific, USA), 1% penicillin/streptomycin (Sigma-Aldrich, USA), under a humid atmosphere (37°C, 5% CO2, 95% air). Cell viability was determined by 3-(4,5-dimethylthiazolyl)-2,5-diphenyltetrazolium bromide (MTT) assay, which detects the reduction of MTT (Sigma-Aldrich, USA) by mitochondrial dehydrogenase to blue formazan product. This reflects the normal function of mitochondria and, hence, cell viability. Briefly, different numbers of cells were seeded in 96-well plates for each time point, in the specific 10^4 cells/well for the 24 h, 7.5×10^3 for 48 h, and 5×10^3 for 72 h were seeded in 96-well plates and incubated at 37 °C, 5% CO_2, for 24 h. The day after, cells were treated with EMEM containing the selected doses of DTXL and DTXL-DPN (0.1–1,000 nM). After 24, 48, and 72 h, the treatment solution was removed and replaced by MTT solutions, according to the manufacturer's instructions. The resulting formazan crystals were then dissolved in ethanol (200 μL/well) and the absorbance was read at 570 nm using a microplate reader (Tecan, CH). Six replicates were considered for each DTXL concentration. Data were collected when the absorbance ranged between 0.8 and 1.2. Cell viability was normalized to that of untreated cells.

Cell uptake experiments. To assess DPN internalization, 4×10^4 MDA-MB-231 were seeded into 8 well cover slides and treated with the DPN at a concentration of 10 DPN/cell. After 2, 4, 8, and 24 h of incubation, cells were fixed using 4% paraformaldehyde and DPN uptake was studied via Z-stacks analysis performed on a Nikon confocal fluorescent microscope. For these studies, RhB-DPN were used.

Histological analysis. After harvesting, organs were fixed in 4% paraformaldehyde (PFA) for 1 day at 4 °C, immersed in a 30% (w/v) sucrose solution for 2 days, and frozen by liquid nitrogen, avoiding direct contact.

Organs were then frozen sectioned using a microtome-cryostat in 20 μm slices. The sections were then placed on HistoBond® microscope slides (Marienfeld, Germany) and stained with 4',6-diamidion-2-phenylindole (DAPI) and CD31 antibody (eBioscience, 1:50 dilution) for vasculature recognition. Slices were imaged using a confocal microscopy (Nikon A1)

Biodistribution studies. MDA-MB-231 luciferase positive cells were injected in the 3rd mammary fat pad of female CD1 immunodeficient nude mice to allow the development of orthotopic breast cancer. Once tumors reached an average radiance in the order of 10^8 p/s/cm²/sr, mice were randomly divided in three groups. Group 1 (n = 3) received 2 mg/kg free DTXL, group 2 (n = 3) received 2 mg/kg multi-passage DTXL-DPN, group 3 (n = 3) received DOTA-Gd-DPN. Each formulation was diluted in saline solution and administered through retro-orbital injection. Mice were sacrificed 24 h post injection and the collected organs were weighed and stored at −80 °C until further analysis. Liquid chromatography-mass spectrometry (LC-MS/MS) was used to quantify the amount of docetaxel accumulated into the organs. Specifically, organs were washed, diluted at a 1:10 w/v ratio in PBS plus 1% of protease inhibitor and homogenized by using a T10 basic ultra-turrax (IKA Technology). For all the samples, 200 μL of tissue homogenate were crashed with an equal volume of acetonitrile containing paclitaxel (300 nM), as internal standard, vortexed for 1 min and centrifuged at 3,000× g at 4 °C for 10 min.

The quantification of DTXL was performed using Waters XEVO TQMS triple quadrupole spectrometer, using Acquity UPLC System (both from Waters). Source of ionization electrospray in positive ion mode ESI(+). For the Chromatography separation was used a column acquity BEH C18 (2.1 mm × 50 mm, 1.7 μm p.s.) with column guard. For the gradient was used: solvent A water + formic acid 0.1%, solvent B acetonitrile + formic acid 0.1%, flow 0.5 mL/min, from 10% of B to 90% in 5 min. The column temperature was maintained at 45 °C and the injection volume was 7 μL. In order to enhance sensitivity and add specificity of identification, MS/MS experiments were

performed using multiple reaction monitoring (MRM) in ESI(+) for DTXL and PTXL.

Inductively coupled plasma mass spectrometry (ICP-MS) (Thermo Fisher) was used to quantify gadolinium in the collected organs. Specifically, organs were weighed and dehydrated through freeze-drying for 2 days. Lyophilized organs were digested through microwave-assisted digestions (MARS 5 Digestion Microwave System). 1 mL of nitric acid (69% HNO_3) and hydrogen peroxide (30% H_2O_2) mixture (ratio 1:3) was used for the digestion.

Optical imaging of orthotopic breast cancer. 0.9 millions of MDA-MB-231 luciferase positive cells were injected in the 3rd mammary fat pad of female CD1 immunodeficient nude mice to allow the development of orthotopic breast cancer. The growth of the tumor mass was followed by whole animal optical imaging (*in vivo* imaging system (IVIS), Perkin-Elmer) until 4 weeks post cells inoculation. Once tumors reached an average radiance in the order of 10^8 p/s/cm^2/sr, mice (n = 4) were intravenously injected with Cy5-DPN. Mice were sacrificed 24 h post injection and *ex vivo* optical imaging was performed to evidence particle tumor accumulation.

Tumor model and therapeutic experiments. All animal experiments were performed according to the guidelines established by the European Communities Council Directive (Directive 2010/63/EU of 22 September 2010) and approved by the National Council on Animal Care of the Italian Ministry of Health. All efforts were made to minimize animal suffering and use the lowest possible number of animals required to produce statistical relevant results, according to the "3Rs concept". For the orthotopic breast tumor model, 6-week old female CD1 immunodeficient nude mice (Charles River, Calco, Italy) were used. Animals were grouped in ventilated cages and able to freely access food and water. They were maintained under controlled conditions: temperature (21 °C ± 2 °C), humidity (50% ± 10%), and light (12 h of light and 12 h of dark). Before cells injection, animals were anaesthetized with a mixture of ketamine (10%) and xylazine (5%), which was administered via a single intraperitoneal injection. For the injection, trypsinized 0.9×10^7 MDA-MB-231 luciferase positive cells were resuspended in cold matrigel solution. A total of 100 µL of matrigel was subcutaneously injected into the third mammary fat gland. Animals were carefully monitored until recovered from anesthesia. Tumor growth was followed by IVIS spectrum system every 2 days, upon intraperitoneal injection of D-luciferin, potassium salt (GoldBio) at a dose of 150 mg/kg and by caliper measurement. Tumor growth was calculated by tumor volume (V) with the formula $V = W^2 \times L/2$ (W = width; L = length). When tumors reached an overall volume of about 0.15 cm^3, mice were randomized into 3 groups (6 mice per group). The groups were dosed for 30 days by retro-orbital injection every 2 days with saline, free-DTXL, and DTXL-DPN. Each injected dose contained 40 µg of DTXL into DPN or as commercial clinical formulation. The therapeutic efficacy of the different treatments was evaluated by whole animal optical imaging (IVIS) and caliper measurement every 2 days. All mice were euthanized when they became moribund or tumor volume passed a volume of 1 cm^3. Survival was monitored and plotted using the Kaplan–Meier method.

Statistical analysis. All data were processed using Excel 2010 software (Microsoft) and GraphPad PRISM. Results are expressed as mean + standard deviation. Statistical analyses on *in vivo* experiments were performed using Student's t-test. Log-rank test was used to test the significance of different survival curves. The p values of <0.05 (*), <0.01 (**), and <0.001 (***) were considered to be statistically significant.

3 Results and discussion

3.1 "Multi-passage" loaded discoidal polymeric nano-constructs

The particle fabrication comprises a number of sequential steps (Fig. 1(a)), through which the "4S" parameters of DPN—size, shape, surface properties, and mechanical stiffness—are precisely tailored in order to optimize their *in vitro* and *in vivo* performance. Briefly, the initial manufacturing step involved the use of a direct laser writing system to realize a silicon master template with billions of wells per wafer presenting a well-defined geometry. In the present study, the wells in the silicon wafer were cylinders with a ~ 1,000 nm in diameter and a ~ 400 nm in depth (Fig. 1(b)). Then, a soft lithographic technique was used to generate multiple negative replicas of the original master template in polydimethylsiloxane (PDMS) (Fig. 1(c)). The wells in the master template were turned into cylindrical posts, comparable in diameter and height to the wells. Finally, the PDMS template was replicated into multiple PVA, sacrificial templates presenting wells with the same geometry as in the master silicon template (Fig. 1(d)).

After drying the PVA template, its wells were accurately filled by uniformly spreading a polymeric paste. This comprised an homogeneous mixture of the hydrophobic PLGA-acid carboxylic terminated (PLGA-COOH) and hydrophilic PEG-DA including the therapeutic and imaging agents of interest. The PLGA-COOH and PEG-DA mixture formed the actual polymeric matrix of DPN, which is characterized by hydrophobic and hydrophilic pockets entrapping the loaded agents. In the current configuration, the chemotherapeutic molecule DTXL and the red fluorescent molecule RhB-DSPE or the near-infra red molecule Cy5-DSPE were dispersed within the polymer matrix. To release and collect the DPN loaded with DTXL and

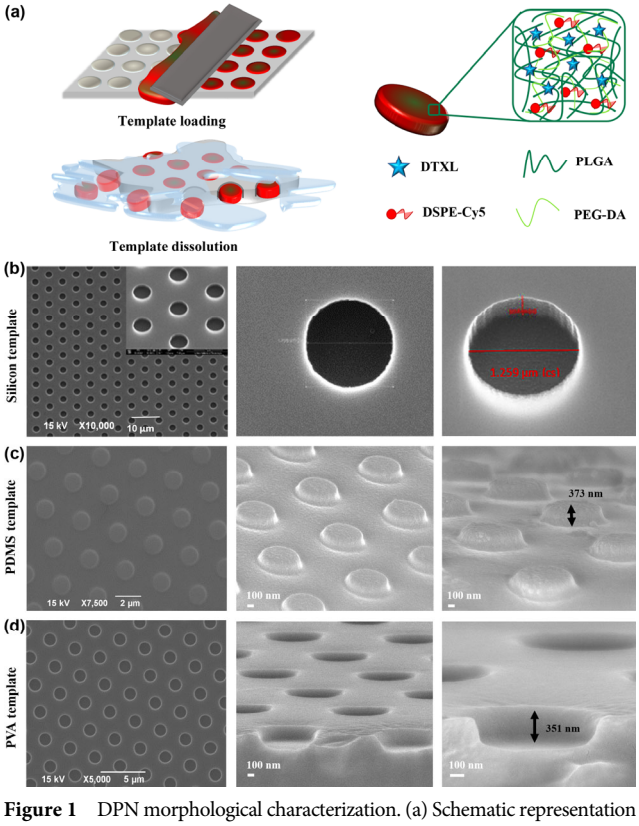

Figure 1 DPN morphological characterization. (a) Schematic representation of the DPN fabrication and purification process (left) and structure and molecular constituents of DPN (right). SEM images of (b) silicon master template; (c) PDMS intermediate template; (d) PVA sacrificial template.

Cy5-DSPE, the PVA templates were dissolved in water for 3 h at room temperature and under gentle stirring (Fig. 1(a)). Differently from the previous authors' practice [51], in this work, the spreading of the polymeric paste on the PVA template was performed multiple times till complete solvent evaporation (4–5 times). This modification in the fabrication protocol, named "multi-passage" loading, allowed the authors to increase the amounts of loaded agents per particle and, thus, improve the DPN pharmacological and imaging properties as compared to the previous configuration ("single-passage" loading).

The morphological properties of the "multi-passage" loaded DPN were investigated using SEM (Fig. 2(a)), TEM (Fig. 2(b)), and confocal fluorescent microscopy (Fig. 2(c)). As compared to the "single-passage" method, the electron and optical density of the "multi-passage" DPN were higher suggesting a larger mass of polymers and fluorescent imaging probes trapped within the matrix, as can be inferred by looking at Figs. 2(b) and 2(c), and Figs. S1(a) and S1(b) in the Electronic Supplementary Material (ESM). The DPN morphological and physico-chemical properties were also characterized by using a Multisizer Particle Counter and a Zetasizer Nano (Figs. 2(d) and 2(e)). The Multisizer Particle Counter spectrum for the "multi-passage" DPN showed a sharp peak around 700 nm ± 150 nm that is slightly, but not significantly (p = 0.1) larger than for the "single-passage" DPN (670 nm ± 100 nm) ("single-passage": purple; "multi-passage": blue in Fig. 2(d)).

This again would imply that the "multi-passage" strategy allows for a more accurate filling of the PVA wells with the polymer and functional agents without changing DPN geometrical proprieties. The dynamic light scattering (DLS) analysis (Fig. 2(e)) showed a uniform and monodispersed size distribution for the "multi-passage" DPN around 880 nm ± 200 nm and a negative surface charge ζ of –32 mV ± 0.15 mV, ensuring the colloidal stability of the suspension. Even the DLS analysis confirmed a small difference in size between the "single-passage" and "multi-passage" DPN design (p = 0.5) ("single-passage": purple; "multi-passage": blue in Figs. 2(d) and 2(e)). Therefore, the "multi-passage" does not alter significantly the morphological and physico-chemical properties of DPN. However, the "multi-passage" DPN were characterized by a significantly higher mechanical stiffness as determined via indentation analyses. Specifically, Fig. 2(e) shows that the apparent Young's modulus for the "multi-passage" DPN is about two times higher than for the conventional "single-passage" DPN. This was expected as the "multi-passage" allows for a higher polymer mass to be deposited within the same PVA well, thus leading to overall more compact and stiffer nanoconstructs.

3.2 Controlled drug release and *in vitro* cytotoxicity.

So far, RhB-DSPE was consistently loaded into DPN to highlight the particle morphological features via fluorescent microscopy. Following the same strategy, any other imaging agent and therapeutic molecule could be directly loaded into the polymeric matrix of DPN. Thus, the chemotherapeutic drug DTXL was dispersed directly within the polymer paste and loaded into DPN. The encapsulation efficiency (EE%) and release profile of DTXL over time are presented in Figs. 3(a) and 3(b), as derived by HPLC. A direct comparison between the "single-passage" and "multi-passage" strategies documents a two-fold increase in drug loading retuning a 10 μg vs. 20 μg of DTXL per 10^9 DPN, respectively. Interestingly, by introducing a simple variation in the fabrication protocol, a two-fold increase in drug loading was achieved. Therefore, the additional passages of the polymeric paste over the PVA template mainly help to fill more homogenously the discoidal wells and, thus, increase the amount of polymer and drug molecules encapsulated per particle.

Then, release studies were performed by incubating DTXL-DPN into phosphate buffered saline (PBS) (infinite sink condition: 4 L) up to 72 h at pH 7.4 and 6.5, representing the mildly acidic environmental conditions of the tumor microenvironment. Figure 3(b) shows the release curves for the "multi-passage" DTXL-DPN. Under physiological conditions (pH 7.4), despite a moderate burst within the first few hours (30% in 1 h), which is most likely related to DTXL molecules adsorbed on the DPN surface, drug release appeared to be sustained overtime up to 72 h. At 24 h, almost 80% of the loaded DTXL was released, and this percentage grew to 85% and 90% at 48 and 72 h, respectively. As expected, drug release was accelerated under acidic conditions for the partial degradation

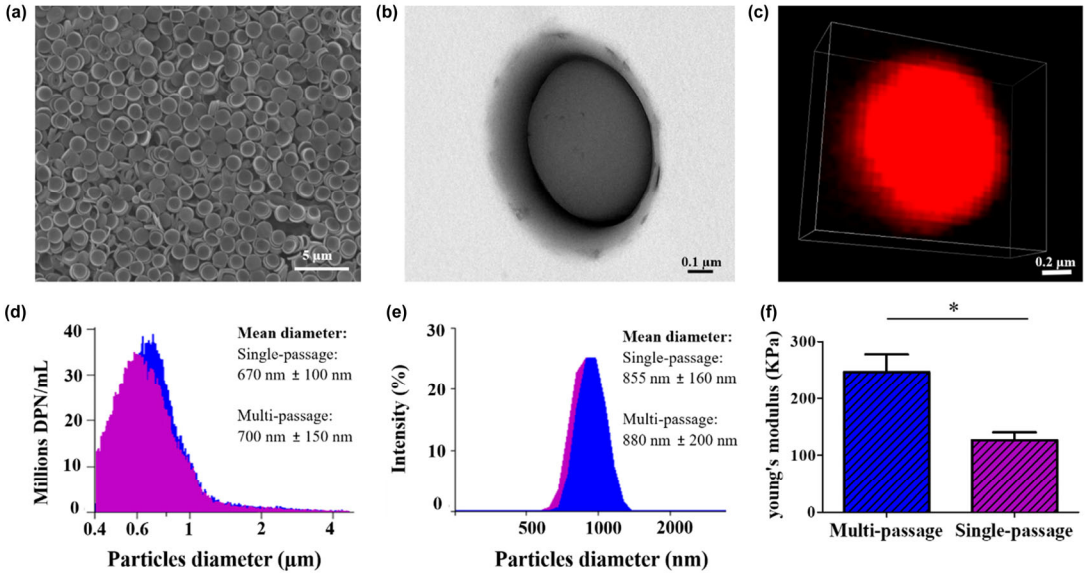

Figure 2 DPN morphological characterization. (a) SEM of DPN. (b) TEM of a single DPN. (c) Confocal fluorescent microscopy of a DPN loaded with rhodamine B–DSPE. (d) Size distribution and DPN measured via a Multisizer Coulter Counter system (1.6 × 10^9 DPN/mL). (e) DPN size distribution measured via DLS. (f) Apparent Young's modulus of DPN measured via nanoindentation (purple bar: "single-passage" vs. blue bar: "multi-passage"; $p < 0.05$).

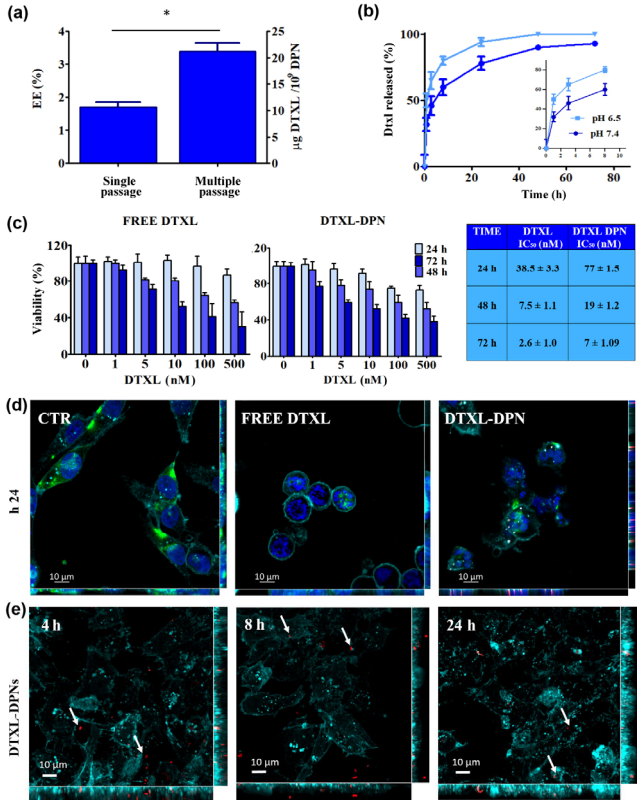

Figure 3 Pharmacological characterization and *in vitro* therapeutic properties of DPN. (a) DTXL amounts and encapsulation efficiencies (EE%) for DPN loaded using the "single-passage" vs. the "multi-passage" strategy. (b) DTXL release out of "multi-passage" DPN over time under physiological (pH 7.4) and acidic (pH 6.5) conditions. (c) Cytotoxic potential on triple negative breast cancer MDA-MB 231 cells treated with Free DTXL and DTXL-DPN up to 72-h incubation time (left). Table listing the IC_{50} values for each treatment condition and time point (right). (d) Confocal fluorescent microscopy images of untreated (left); free DTXL treated (center); DTXL-DPN treated MDA-MB 231 cells (20 nM DTXL, at 24 h). (e) Confocal fluorescent microscopy images of MDA-MB 231 cells incubated with DPN labeled with RhB-DSPE (red) and loaded with curcumin (green) at different time point (4, 8, and 24 h).

of the DPN matrix [53]. Specifically, at pH 6.5, 90% of the drug was released within 24 h while it took 72 h to completely release all loaded DTXL. The proposed "multi-passage" direct loading strategy allowed the authors to improve the pharmacological properties of DPN reaching drug loading conditions that are compatible with tumor treatment. However, the "multi-passage" DPN are characterized by higher loading and a slower release rate as compared to the "single-passage" configuration.

Finally, the *in vitro* cell-killing efficacy of "multi-passage" DPN was tested against a triple negative breast cancer cell line, namely the MDA-MB 231 cells. These were incubated with different concentrations of DTXL-DPN to estimate the IC_{50} values at 24, 48, and 72 h. Figure 3(c) shows the percentage of viable cells as a function of free and DPN-loaded DTXL concentrations. As expected, DTXL-DPN were less cytotoxic on tumor cells as compared to free DTXL molecules for a given time, documenting an IC_{50} value of 77 nM ± 1.5 nM against 38.50 nM ± 3.3 nM at 24 h. Similarly, at longer time points (72 h), the particle formulation confirmed a slightly lower toxicity than the free drug with an IC_{50} value of 7 nM ± 1.09 nM against 2.6 nM ± 1.0 nM. Data are presented in Fig. 3(c) in graphical and tabular forms. The controlled release of DTXL from the DPN is indeed responsible for the lower efficacy of the DTXL-DPN for any given time point. However, the cytotoxic potential of free DTXL is essentially preserved upon encapsulation into DPN. Note that no toxicity was associated with empty DPN even at the highest concentration of 800 DPN/cell (Fig. S2 in the ESM). Furthermore, the pharmacological activity on cytoskeletal microtubules was assessed by confocal microscopy as showed in Fig. 3(d). The untreated MDA-MB 231 displayed a well-organized microtubule cytoskeleton (green) and a typical, elongated shape. On the contrary, cells treated with free DTXL and DTXL-DPN (20 nM) presented microtubule bundles and aberrant mitotic multinucleated morphologies already at 24 h post incubation. Moreover, confocal microscopy was used to assess further DPN interaction with MDA-MB 231 at 2, 4, 8, and 24 h for the concentration of 10 DPN/cell. Representative images in Fig. 3(e) proved that just a few particles were internalized while most DPN sat on or next to the cell membrane releasing thereof the therapeutic cargo.

3.3 Preclinical imaging and therapeutic performance of DTXL-DPN

To evaluate the therapeutic performance of DTXL-DPN, an orthotopic murine model of TBNC was considered. Figure 4(a) reports schematically the timeline of the preclinical experiments. Initially, MDA-MB-231 Luc^+ cells were injected into the 3rd mammary fat pad of 7-week old immunodeficient mice and left to proliferate for 45 days to establish a palpable tumor mass. Tumor growth was monitored by whole animal optical bioluminescence imaging (IVIS) and manually with a caliper. Upon reaching an average tumor size of 0.15 cm^3, mice were randomly divided in three experimental groups: the "saline" group, including mice injected with PBS; the "free-DTXL" group, including mice injected with a DTXL solution (2 mg/kg); and the "DTXL-DPN" group, including mice treated with 2 mg/kg DTXL-loaded within the DPN. In all the cases, the agent administration was performed intravenously every 2 days for up to 30 days, returning a total number of injections equals to 13. Note that the DTXL administered dose of 2 mg/kg was significantly lower than that conventionally used in pre-clinical experiments, which typically ranges between 10 and 20 mg/kg.

Figure 4(b) summarized the tumor growth curves for the three different treatment groups over a period of 120 days. Malignant masses in the "saline" group (black line) continuously grew over time reaching an average size of 1.16 cm^3 ± 0.14 cm^3 at about 90 days, at which time the surviving mice (only 2) were sacrificed. Mice treated with systemically administered free-DTXL (red line) showed an initial positive response to therapy with a stabilization of the tumor mass within the first 3 weeks of treatment, then followed by a progressive growth demonstrating relapsing of the disease. The mice that survived at 120 days (n = 2) showed an average malignant mass of 0.74 cm^3 ± 0.57 cm^3. The "DTXL-DPN" group (blue line) showed an overall positive response to the treatment with a significant tumor stabilization during the whole observation period. As documented in Fig. 4(b), a moderate increase in tumors size was observed during the first 70 days up to an average volume of 0.48 cm^3 ± 0.4 cm^3 that was then followed by a steady decrease for the remain observation period below the original tumor size.

Note that even in the initial phase, the tumor growth rate was lower for the mice treated with DTXL-DPN rather than with free-DTXL. Figure S3 in the ESM reports the tumor growth curves for each, single animal and experimental group, based on direct caliper measurements as well as average bioluminescence radiance. Mouse survival is plotted in Fig. 4(c). The three curves demonstrate that 80% of the DTXL-DPN

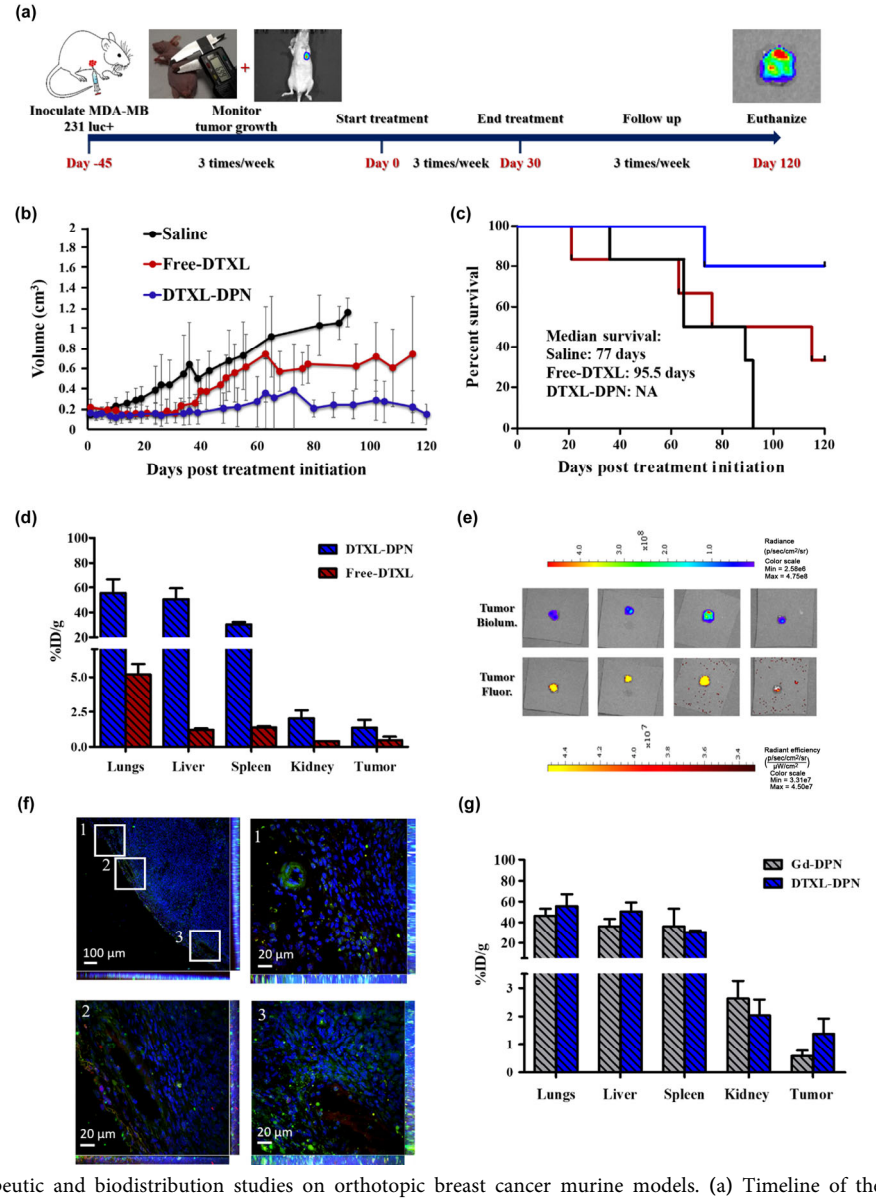

Figure 4 *In vivo* therapeutic and biodistribution studies on orthotopic breast cancer murine models. (a) Timeline of the preclinical experiments performed on mice bearing orthotopic breast cancer and including bioluminescence/fluorescent imaging and tumor growth analysis. (b) Average tumor growth curves. Data are presented as the average tumor volume ± SD. At 120 days: $p < 0.05$ for free DTXL vs. saline and DTXL-DPN vs. saline; and $p = 0.05$ for DTXL-DPN vs. DTXL. At 92 days: $p < 0.05$ for DTXL-DPN vs. DTXL, $n \geq 5$. (c) Kaplan–Meier curves for survival (black line: saline; red line: free DTXL; blue line: DTXL-DPN). (d) DTXL accumulation in major organs expressed as the percentage of the injected dose normalized by the organ mass (%ID/g) at 24 h post administration of free-DTXL (red bar) and DTXL-DPN (blue bar) (2 mg/kg of DTXL). (e) *Ex vivo* bioluminescence and fluorescence analysis for tumors harvested at 24 h post Cy5-DPN injection. (f) Localization of Cy5-DPN (red spot) in the tumor vasculature (aCD31 staining in in green). (g) Gadolinium (grey bar) and DTXL (blue bar) accumulation in major organs expressed as the percentage of the injected dose normalized by the organ mass (%ID/g) at 24 h post systemic administration of Gd-DPN and DTXL-DPN, respectively.

mice survived at 120 days against the 30% for the free-DTXL case. The control mice were sacrificed within 90 days because of excessive tumor burden. The difference between average tumor volumes for DTXL-DPN and free-DTXL was statistically significant at day 92 ($p = 0.02$), representing the end point for the saline group, and at day 120 ($p = 0.05$), indicating the end of the study. The average radiance associated with the tumors of the surviving animals at the end of the treatment are reported in Figs. S4(a) and S4(b) in the ESM, documenting once again the smaller size of the DTXL-DPN treated tumors over the free-DTXL group.

To further characterize the improved therapeutic performance of the "multi-passage" DTXL-DPN over the free-DTXL, the tissue-specific accumulation of DTXL and Gd-DPN was assessed in tumor bearing mice. Using LC-MS, the amounts of DTXL at 24 h post injection were quantified in different organs. Data are presented in Fig. 4(d) in terms of percentage of the injected dose per mass organ (%ID/g) for the free-DTXL (red column) and DTXL-DPN (blue column). The amount of DTXL deposited within the tumor mass following a single DTXL-DPN injection (1.4 %ID/g ± 0.6 %ID/g) is about 3 times higher than that measured for the free-DTXL (0.5 %ID/g ± 0.2 %ID/g). This indeed would explain the enhanced therapeutic efficacy observed for the DTXL-DPN over the free DTXL in Figs. 4(b) and 4(c). Furthermore, the intratumor accumulation of the systemically administered DPN was also confirmed by *in vivo* optical imaging upon loading the nanoconstructs with the near-infrared compound DSPE-Cy5. This is presented in Fig. 4(e) that shows, side by side, the bioluminescence signal of the MDA-MB-231 Luc$^+$ tumor cells (top panel) and the fluorescence signal associated with the Cy5-DPN (bottom panel) confirming the intratumor accumulation of the polymeric

nanoconstructs. At a higher magnification scale, the histological images of Fig. 4(f) document the localization of the Cy5-DPN (red dots) mostly on the surface of the blood vessels feeding the malignant mass (blue color: cell nuclei; green color: CD31 staining of the capillary endothelial cells). Note that, given their characteristic sub micrometric size, the 1,000 nm × 400 nm DPN were not expected to diffuse deep into the malignant tissue but rather deposit over the vascular surface [42].

The bar charts in Fig. 4(d) and Table S1 in the ESM report that a significant amount of DTXL was also associated with the lungs (55.5 %ID/g ± 11 %ID/g), in addition to the liver (50.5 %ID/g ± 7 %ID/g) and spleen (30.4 %ID/g ± 1.7 %ID/g) of the animals injected with DTXL-DPN. This was also observed via fluorescence imaging when monitoring the organ-specific accumulation of Cy5-DPN over time (Figs. S5 and S6 in the ESM). The pulmonary accumulation of the "multi-passage" DPN should be ascribed to their increased mechanical stiffness, which would favor geometrical entrapment in the smallest capillary beds of the lungs, as previously document by other authors [54, 55]. However, as seen in the tumor mass (Fig. 4(f)), the DPN tend to deposit on the surface of the pulmonary vasculature (Fig. S7 in the ESM). Based on this observation, one could hypothesize that the "multi-passage" DTXL-DPN in the lungs could act as a vascular depot of DTXL, slowly releasing the chemotherapeutic drug in the vasculature to benefit eventually the tumor mass. Following this line of though, DPN were loaded with Gd(DOTA)-DPSE so that their biodistribution could be readily assessed by measuring the Gd content in each organ via inductively coupled plasma mass spectrometry (ICP-MS). The bar chart in Fig. 4(g) gives the percentage of the injected dose of Gd accumulating in a specific organ, normalized by the organ mass (%ID/g), and compares it with the DTXL accumulation in mice injected with DTLX-DPN. Therefore, in Fig. 4(g), the Gd bar (gray bar) returns the DPN tissue deposition whereas the DTXL bar (blue bar) provides the actual DTXL accumulation. Note that Gd is stably loaded into the DPN with a release rate lower than 10% at 24 h (Fig. S8 in the ESM). Also, almost 80% of the injected DTXL and Gd are recovered by analyzing their deposition in multiple major organs at 24 h, thus confirming the accuracy of the analyses (Tables S1 and S2 in the ESM). This direct comparison shows that while the DTXL and Gd accumulation in the lungs, liver, spleen, and kidneys are quite comparable, the tumor accumulation of DTXL is about 3 times higher than that of Gd. This would suggest that the amount of DTXL recovered in the malignant mass at 24 h post injection is partly associated with the direct accumulation of DTXL-DPN in the tumor and partly related to the sustained release of DTXL from "multi-passage" DPN lodging along the vascular network of the lungs and possibly other organs.

It is here important to notice that the DTXL accumulation in the lungs and other organs does not appear to have any chronic effect on the behavior of the animals. This was documented by monitoring the mouse weight over the whole duration of the experiment (Fig. S9 in the ESM). Free-DTXL and DTXL-DPN treatments caused a negligible reduction (10%) in mouse weight over the first 20 days. As the treatment was completed, all mice progressively regained the lost weight and, at 120 days, no difference was observed as compared to the initial point. Overall, the treatment with DPN was well tolerated by the mice and the moderate loss of weight should be mostly attributed to the drug inherent toxicity.

Overall, the enhanced tumor accumulation and sustained drug release from the vascular-localized DPN would explain the higher therapeutic efficacy associated with the DTXL-DPN in treating triple negative breast cancer over the conventional molecular formulation. It is here important to highlight that animals were injected every 2 days for 13 consecutive times with only 2 mg/kg of DTXL. This was sufficient to modulate the growth of orthotopic TNBC during the first 70 days and, eventually, induce tumor regression in the following 50 days. This resulted in an 80% survival for DTXL-DPN as compared to 30% for the free-DTXL treatment. Conventionally, in these preclinical studies, DTXL doses ranging between 10 and 50 mg/kg of animal are considered [33, 36, 56]. Finally, it should be also noted that given the characteristic size of 1,000 nm × 400 nm, DPN are not expected to cross the fenestrated endothelium and migrate into a perivascular position as most nanomedicine do. In this sense, DPN do not rely on the EPR effect to deposit within malignant masses but would rather mimic the vascular behavior of platelets, thus confirming the importance of bioinspiration and biomimicry in the development of novel drug delivery systems [49].

4 Conclusions

In conclusions, it has been demonstrated that DPN can be loaded with therapeutic agents to realize a drug delivery system capable to treat triple negative breast cancers. A potent chemotherapeutic agent—DTXL—and imaging compounds—Cy5 and Gd (DOTA) conjugated to a lipid chain—were efficiently entrapped into the hydrogel matrix of DPN using a "multi-passage" direct loading strategy. Independently of the enhanced permeability and retention effect, the geometrical and mechanical attributes of the "multi-passage" DPN favored high tumor deposition of DTXL as compared to the freely administered drug. This supported tumor regression even at minimal injected drug doses. These results continue to support the notion that effective tumor treatment can be achieved even without relying on the EPR effect. DPN could be used together with conventional nanomedicines and small anti-cancer molecules against a variety of malignancies.

Competing interests

The authors have declared that no competing interest exists.

Acknowledgments

The authors wish to thank the reviewers for their valuable comments and suggestions to improve the quality of the paper. This project was partially supported by the European Research Council, under the European Union's Seventh Framework Programme (FP7/2007-2013)/ERC grant agreement No. 616695, by the Italian Association for Cancer Research (AIRC) under the individual investigator grant No. 17664, and by the European Union's Horizon 2020 research and innovation programme under the Marie Skłodowska-Curie grant agreement No. 754490. The authors acknowledge the precious support provided by the Nikon Center, the Material Characterization Facility, the electron microscopy and nanofabrication facilities at the Italian Institute of Technology, and the work of Luca Caseracciu for the mechanical characterization of DPN.

Funding note: Open Access funding provided by Università degli Studi di Genova.

Electronic Supplementary Material: Supplementary material (further details of morphological differences between single

and multi-passage DPN, *in vitro* and *in vivo* therapeutic efficacy) is available in the online version of this article at https://doi.org/10.1007/s12274-021-3507-8.

References

[1] Perou, C. M.; Sørlie, T.; Eisen, M. B.; van de Rijn, M.; Jeffrey, S. S.; Rees, C. A.; Pollack, J. R.; Ross, D. T.; Johnsen, H.; Akslen, L. A. et al. Molecular portraits of human breast tumours. *Nature* **2000**, *406*, 747–752.

[2] Foulkes, W. D.; Smith, I. E.; Reis-Filho, J. S. Triple-negative breast cancer. *N. Engl. J. Med.* **2010**, *363*, 1938–1948.

[3] Sørlie, T.; Perou, C. M.; Tibshirani, R.; Aas, T.; Geisler, S.; Johnsen, H.; Hastie, T.; Eisen, M. B.; van de Rijn, M.; Jeffrey, S. S. et al. Gene expression patterns of breast carcinomas distinguish tumor subclasses with clinical implications. *Proc. Natl. Acad. Sci. USA* **2001**, *98*, 10869–10874.

[4] Kennecke, H.; Yerushalmi, R.; Woods, R.; Cheang, M. C. U.; Voduc, D.; Speers, C. H.; Nielsen, T. O.; Gelmon, K. Metastatic behavior of breast cancer subtypes. *J. Clin. Oncol.* **2010**, *28*, 3271–3277.

[5] Bianchini, G.; Balko, J. M.; Mayer, I. A.; Sanders, M. E.; Gianni, L. Triple-negative breast cancer: Challenges and opportunities of a heterogeneous disease. *Nat. Rev. Clin. Oncol.* **2016**, *13*, 674–690.

[6] Lee, A.; Djamgoz, M. B. A. Triple negative breast cancer: Emerging therapeutic modalities and novel combination therapies. *Cancer Treat. Rev.* **2018**, *62*, 110–122.

[7] Chavez, K. J.; Garimella, S. V.; Lipkowitz, S. Triple negative breast cancer cell lines: One tool in the search for better treatment of triple negative breast cancer. *Breast Dis.* **2010**, *32*, 35–48.

[8] Anders, C. K.; Carey, L. A. Biology, metastatic patterns, and treatment of patients with triple-negative breast cancer. *Clin. Breast Cancer* **2009**, *9*, S73–S81.

[9] Bourgeois-Daigneault, M. C.; Roy, D. G.; Aitken, A. S.; El Sayes, N.; Martin, N. T.; Varette, O.; Falls, T.; St-Germain, L. E.; Pelin, A.; Lichty, B. D. et al. Neoadjuvant oncolytic virotherapy before surgery sensitizes triple-negative breast cancer to immune checkpoint therapy. *Sci. Transl. Med.* **2018**, *10*, eaao1641.

[10] Isakoff, S. J. Triple-negative breast cancer: Role of specific chemotherapy agents. *Cancer J.* **2010**, *16*, 53–61.

[11] Cleator, S.; Heller, W. Coombes, R. C. Triple-negative breast cancer: Therapeutic options. *Lancet Oncol.* **2007**, *8*, 235–244.

[12] Kloover, J. S.; den Bakker, M. A.; Gelderblom, H.; van Meerbeeck, J. P. Fatal outcome of a hypersensitivity reaction to paclitaxel: A critical review of premedication regimens. *Br. J. Cancer* **2004**, *90*, 304–305.

[13] Gelderblom, H.; Verweij, J.; Nooter, K.; Sparreboom, A. Cremophor EL: The drawbacks and advantages of vehicle selection for drug formulation. *Eur. J. Cancer* **2001**, *37*, 1590–1598.

[14] Laurentiis, M. D.; Cancello, G.; D'Agostino, D.; Giuliano, M.; Giordano, A.; Montagna, E.; Lauria, R.; Forestieri, V., Esposito, A.; Silvestro, L. et al. Taxane-based combinations as adjuvant chemotherapy of early breast cancer: A meta-analysis of randomized trials. *J. Clin. Oncol.* **2008**, *26*, 44–53.

[15] Engels, F. K.; Mathot, R. A.; Verweij, J. Alternative drug formulations of docetaxel: A review. *Anti-Cancer Drugs* **2007**, *18*, 95–103.

[16] van der Meel, R.; Sulheim, E.; Shi, Y.; Kiessling, F.; Mulder, W. J. M.; Lammers, T. Smart cancer nanomedicine. *Nat. Nanotechnol.* **2019**, *14*, 1007–1017.

[17] Yu, M. K.; Park, J.; Jon, S. Targeting strategies for multifunctional nanoparticles in cancer imaging and therapy. *Theranostics* **2012**, *2*, 3–44.

[18] Gradishar, W. J.; Tjulandin, S.; Davidson, N.; Shaw, H.; Desai, N.; Bhar, P.; Hawkins, M.; O'Shaughnessy, J. Phase III trial of nanoparticle albumin-bound paclitaxel compared with polyethylated castor oil–based paclitaxel in women with breast cancer. *J. Clin. Oncol.* **2005**, *23*, 7794–7803.

[19] Anselmo, A. C.; Mitragotri, S. Nanoparticles in the clinic: An update. *Bioeng. Transl. Med.* **2019**, *4*, e10143.

[20] Maeda, H.; Nakamura, H.; Fang, J. The EPR effect for macromolecular drug delivery to solid tumors: Improvement of tumor uptake, lowering of systemic toxicity, and distinct tumor imaging *in vivo*. *Adv. Drug Deliv. Rev.* **2013**, *65*, 71–79.

[21] Golombek, S. K.; May, J. N.; Theek, B.; Appold, L.; Drude, N.; Kiessling, F.; Lammers, T. Tumor targeting via EPR: Strategies to enhance patient responses. *Adv. Drug Deliv. Rev.* **2018**, *130*, 17–38.

[22] Esmaeili, F.; Dinarvand, R.; Ghahremani, M. H.; Amini, M.; Rouhani, H.; Sepehri, N.; Ostad, S. N.; Atyabi, F. Docetaxel–albumin conjugates: Preparation, *in vitro* evaluation and biodistribution studies. *J. Pharm. Sci.* **2009**, *98*, 2718–2730.

[23] Immordino, M. L.; Brusa, P.; Arpicco, S.; Stella, B.; Dosio, F.; Cattel, L. Preparation, characterization, cytotoxicity and pharmacokinetics of liposomes containing docetaxel. *J. Control. Release* **2003**, *91*, 417–429.

[24] Chan, J. M.; Zhang, L. F.; Yuet, K. P.; Liao, G.; Rhee, J. W.; Langer, R.; Farokhzad, O. C. PLGA–lecithin–PEG core–shell nanoparticles for controlled drug delivery. *Biomaterials* **2009**, *30*, 1627–1634.

[25] Hwang, H. Y.; Kim, I. S.; Kwon, I. C.; Kim, Y. H. Tumor targetability and antitumor effect of docetaxel-loaded hydrophobically modified glycol chitosan nanoparticles. *J. Control. Release* **2008**, *128*, 23–31.

[26] Tan, L. W.; Peng, J. R.; Zhao, Q.; Zhang, L.; Tang, X. C.; Chen, L. J.; Lei, M. Y.; Qian, Z. Y. A novel MPEG-PDLLA-PLL copolymer for docetaxel delivery in breast cancer therapy. *Theranostics* **2017**, *7*, 2652–2672.

[27] Gaucher, G.; Marchessault, R. H.; Leroux, J. C. Polyester-based micelles and nanoparticles for the parenteral delivery of taxanes. *J. Control. Release* **2010**, *143*, 2–12.

[28] Huynh, L.; Leroux, J. C.; Allen, C. Enhancement of docetaxel solubility via conjugation of formulation-compatible moieties. *Org. Biomol. Chem.* **2009**, *7*, 3437–3446.

[29] Sun, B. Y.; Straubinger, R. M.; Lovell, J. F. Current taxane formulations and emerging cabazitaxel delivery systems. *Nano Res.* **2018**, *11*, 5193–5218.

[30] Pillai, G. Nanomedicines for cancer therapy: An update of FDA approved and those under various stages of development. *SOJ Pharm. Pharm. Sci.* **2014**, *1*, 13.

[31] Hawkins, M. J.; Soon-Shiong, P.; Desai, N. Protein nanoparticles as drug carriers in clinical medicine. *Adv. Drug Deliv. Rev.* **2008**, *60*, 876–885.

[32] Ernsting, M. J.; Murakami, M.; Undzys, E.; Aman, A.; Press, B.; Li, S. D. A docetaxel-carboxymethylcellulose nanoparticle outperforms the approved taxane nanoformulation, Abraxane, in mouse tumor models with significant control of metastases. *J. Control. Release* **2012**, *162*, 575–581.

[33] Bowerman, C. J.; Byrne, J. D.; Chu, K. S.; Schorzman, A. N.; Keeler, A. W.; Sherwood, C. A.; Perry, J. L.; Luft, J. C.; Darr, D. B.; Deal, A. M. et al. Docetaxel-loaded PLGA nanoparticles improve efficacy in taxane-resistant triple-negative breast cancer. *Nano Lett.* **2017**, *17*, 242–248.

[34] Contreras-Cáceres, R.; Leiva, M. C.; Ortiz, R.; Díaz, A.; Perazzoli, G.; Casado-Rodríguez, M. A.; Melguizo, C.; Baeyens, J. M.; López-Romero, J. M.; Prados, J. Paclitaxel-loaded hollow-poly (4-vinylpyridine) nanoparticles enhance drug chemotherapeutic efficacy in lung and breast cancer cell lines. *Nano Res.* **2017**, *10*, 856–875.

[35] Huang, J. B.; Zhang, H.; Yu, Y.; Chen, Y.; Wang, D.; Zhang, G. Q.;

Zhou, G. C.; Liu, J. J.; Sun, Z. G.; Sun, D. X. et al. Biodegradable self-assembled nanoparticles of poly (D, L-lactide-co-glycolide)/ hyaluronic acid block copolymers for target delivery of docetaxel to breast cancer. *Biomaterials* **2014**, *35*, 550–566.

[36] Liang, D. S.; Zhang, W. J.; Wang, A. T.; Su, H. T.; Zhong, H. J.; Qi, X. R. Treating metastatic triple negative breast cancer with CD44/ neuropilin dual molecular targets of multifunctional nanoparticles. *Biomaterials* **2017**, *137*, 23–36.

[37] Li, S. H.; Goins, B.; Hrycushko, B. A.; Phillips, W. T.; Bao, A. Feasibility of eradication of breast cancer cells remaining in postlumpectomy cavity and draining lymph nodes following intracavitary injection of radioactive immunoliposomes. *Mol. Pharmaceutics* **2012**, *9*, 2513–2522.

[38] Wilhelm, S.; Tavares, A. J.; Dai, Q.; Ohta, S.; Audet, J.; Dvorak, H. F.; Chan, W. C. W. Analysis of nanoparticle delivery to tumours. *Nat. Rev. Mater.* **2016**, *1*, 16014.

[39] Petersen, A. L.; Hansen, A. E.; Gabizon, A.; Andresen, T. L. Liposome imaging agents in personalized medicine. *Adv. Drug Deliv. Rev.* **2012**, *64*, 1417–1435.

[40] Moss, J. I.; Barjat, H.; Emmas, S. A.; Strittmatter, N.; Maynard, J.; Goodwin, R. J. A.; Storm, G.; Lammers, T.; Puri, S.; Ashford, M. B. et al. High-resolution 3D visualization of nanomedicine distribution in tumors. *Theranostics* **2020**, *10*, 880–897.

[41] Hauert, S.; Berman, S.; Nagpal, R.; Bhatia, S. N. A computational framework for identifying design guidelines to increase the penetration of targeted nanoparticles into tumors. *Nano Today* **2013**, *8*, 566–576.

[42] Palange, A. L.; Palomba, R.; Rizzuti, I. F.; Ferreira, M.; Decuzzi, P. Deformable discoidal polymeric nanoconstructs for the precise delivery of therapeutic and imaging agents. *Mol. Ther.* **2017**, *25*, 1514–1521.

[43] Kolhar, P.; Anselmo, A. C.; Gupta, V.; Pant, K.; Prabhakarpandian, B.; Ruoslahti, E.; Mitragotri, S. Using shape effects to target antibody-coated nanoparticles to lung and brain endothelium. *Proc. Natl. Acad. Sci. USA* **2013**, *110*, 10753–10758.

[44] Myerson, J. W.; Anselmo, A. C.; Liu, Y. L.; Mitragotri, S.; Eckmann, D. M.; Muzykantov, V. R. Non-affinity factors modulating vascular targeting of nano- and microcarriers. *Adv. Drug. Deliv. Rev.* **2016**, *99*, 97–112.

[45] Key, J.; Palange, A. L.; Gentile, F.; Aryal, S.; Stigliano, C.; Di Mascolo, D.; De Rosa, E.; Cho, M.; Lee, Y.; Singh, J. et al. Soft discoidal polymeric nanoconstructs resist macrophage uptake and enhance vascular targeting in tumors. *ACS Nano* **2015**, *9*, 11628–11641.

[46] Decuzzi, P.; Godin, B.; Tanaka, T.; Lee, S. Y.; Chiappini, C.; Liu, X.; Ferrari, M. Size and shape effects in the biodistribution of intravascularly injected particles. *J. Control. Release* **2010**, *141*, 320–327.

[47] van de Ven, A. L.; Kim, P.; Haley, O.; Fakhoury, J. R.; Adriani, G.; Schmulen, J.; Moloney, P.; Hussain, F.; Ferrari, M.; Liu, X. W. et al. Rapid tumoritropic accumulation of systemically injected plateloid particles and their biodistribution. *J. Control. Release* **2012**, *158*, 148–155.

[48] Adriani, G.; de Tullio, M. D.; Ferrari, M'; Hussain, F.; Pascazio, G.; Liu, X. W.; Decuzzi, P. The preferential targeting of the diseased microvasculature by disk-like particles. *Biomaterials* **2012**, *33*, 5504–5513.

[49] Valcourt, D. M.; Harris, J.; Riley, R. S.; Dang, M. G.; Wang, J. X.; Day, E. S. Advances in targeted nanotherapeutics: From bioconjugation to biomimicry. *Nano Res.* **2018**, *11*, 4999–5016.

[50] Palomba, R.; Palange, A. L.; Rizzuti, I. F.; Ferreira, M.; Cervadoro, A.; Barbato, M. G.; Canale, C.; Decuzzi, P. Modulating phagocytic cell sequestration by tailoring nanoconstruct softness. *ACS Nano* **2018**, *12*, 1433–1444.

[51] Ferreira, M.; Rizzuti, I. F.; Palange, A. L.; Barbato, M. G.; Di Francesco, V.; Di Francesco, M.; Decuzzi, P. Optimizing the pharmacological properties of discoidal polymeric nanoconstructs against triple-negative breast cancer cells. *Front. Bioeng. Biotechnol.* **2020**, *8*, 5.

[52] Colasuonno, M.; Palange, A. L.; Aid, R.; Ferreira, M.; Mollica, H.; Palomba, R.; Emdin, M.; Del Sette, M.; Chauvierre, C.; Letourneur, D. et al. Erythrocyte-inspired discoidal polymeric nanoconstructs carrying tissue plasminogen activator for the enhanced lysis of blood clots. *ACS Nano* **2018**, *12*, 12224–12237.

[53] Key, J.; Aryal, S.; Gentile, F.; Ananta, J. S.; Zhong M.; Landis, M. D.; Decuzzi, P. Engineering discoidal polymeric nanoconstructs with enhanced magneto-optical properties for tumor imaging. *Biomaterials* **2013**, *34*, 5402–5410.

[54] Kutscher, H. L.; Chao, P.; Deshmukh, M.; Singh, Y.; Hu, P. D.; Joseph, L. B.; Reimer, D. C.; Stein, S.; Laskin, D. L.; Sinko, P. J. Threshold size for optimal passive pulmonary targeting and retention of rigid microparticles in rats. *J. Control. Release* **2010**, *143*, 31–37.

[55] Anselmo, A. C.; Modery-Pawlowski, C. L.; Menegatti, S.; Kumar, S.; Vogus, D. R.; Tian, L. L.; Chen, M.; Squires, T. M.; Sen Gupta, A.; Mitragotri, S. Platelet-like nanoparticles: Mimicking shape, flexibility, and surface biology of platelets to target vascular injuries. *ACS Nano* **2014**, *8*, 11243–11253.

[56] Mosallaei, N.; Jaafari, M. R.; Hanafi-Bojd, M. Y.; Golmohammadzadeh, S.; Malaekeh-Nikouei, B. Docetaxel-loaded solid lipid nanoparticles: Preparation, characterization, *in vitro*, and *in vivo* evaluations. *J. Pharm. Sci.* **2013**, *102*, 1994–2004.